Complex apodization Lyot coronagraphy for the direct imaging of exoplanet systems: design, fabrication, and laboratory demonstration

John Trauger*[a], Dwight Moody[a], Brian Gordon[a], John Krist[a], Dimitri Mawet[b]
[a] Jet Propulsion Laboratory, California Institute of Technology, Pasadena, CA 91109 USA
[b] European Southern Observatory, Santiago, Chile

ABSTRACT

We review the design, fabrication, performance, and future prospects for a complex apodized Lyot coronagraph for high-contrast exoplanet imaging and spectroscopy. We present a newly designed circular focal plane mask with an inner working angle of 2.5 λ/D. Thickness-profiled metallic and dielectric films superimposed on a glass substrate provide control over both the real and imaginary parts of the coronagraph wavefront. Together with a deformable mirror for control of wavefront phase, the complex Lyot coronagraph potentially exceeds billion-to-one contrast over dark fields extending to within angular separations of 2.5 λ/D from the central star, over spectral bandwidths of 20% or more, and with throughput efficiencies better than 50%.

Our approach is demonstrated with a linear occulting mask, for which we report our best laboratory imaging contrast achieved to date. Raw image contrasts of 3×10^{-10} over 2% bandwidths, 6×10^{-10} over 10% bandwidths, and 2×10^{-9} over 20% bandwidths are consistently achieved across high contrast fields extending from an inner working angle of 3 λ/D to a radius of 15 λ/D. Occulter performance is analyzed in light of experiments and optical models, and prospects for further progress are summarized.

The science capability of the hybrid Lyot coronagraph is compared with requirements for ACCESS, a representative space coronagraph concept for the direct imaging and spectroscopy of exoplanet systems. This work has been supported by NASA's Strategic Astrophysics Technology / Technology Demonstrations for Exoplanet Missions (SAT/TDEM) program.

1. INTRODUCTION

1.1 Objectives

The TDEM program advances key technologies for a space-based exoplanet mission. Exoplanets in the size range from Earth to Jupiter, when imaged in reflected starlight, will be fainter than their parent stars by factors of 10^{-9} to 10^{-10}. We use ACCESS[1,2], a representative coronagraph mission concept, as context for our technology development. To image exoplanet systems in reflected starlight, a coronagraph system must provide raw image contrast of 10^{-9} or better, and we expect that post-processing of image data will extend detection sensitivities an order of magnitude fainter[3].

ACCESS forms a high contrast "dark field" over a working angle spanning 3–22 λ_0/D. The 3 λ_0/D inner working angle is the outcome of science requirements and coronagraph design, while the outer working angle (~22 λ_0/D) is defined by the highest spatial frequency controlled by a deformable mirror (DM) within the coronagraph with 48 actuators across the pupil diameter D. The dark field of view is characterized as a background of coherent speckles scattered from the central star. Optical modeling has shown that high contrast is hardest to achieve at field angles closest to the target star. This work addresses the most challenging location in the image plane, at the small angular separations required by ACCESS, as well as the behavior of the speckles to the outer extent of the dark field.

Our objectives are to demonstrate that the complex apodized Lyot coronagraph technology is ready, that it produces raw image contrast at the 10^{-9} level or better, and that its performance is stable and repeatable. This mirrors the approach for TPF-C Milestones #1 and #2 [4,5], which respectively demonstrated monochromatic and broadband (10%) starlight suppression in the High Contrast Imaging Testbed (HCIT)[6], but now with a smaller inner working angle and broader spectral bandwidths. Here, spectral bandwidth is defined as the ratio $\delta\lambda/\lambda_0$, where $\delta\lambda$ is the full width at half maximum transmittance of the band-defining optical filter and λ_0 is the central wavelength. The inner and outer working angles (IWA and OWA) are defined in terms of the central wavelength λ_0 and the diameter D of the aperture stop on the deformable mirror (DM), which is the pupil-defining element of the laboratory coronagraph.

Further, the laboratory experiments validate our performance models and verify that the coronagraph behavior is thoroughly understood. Our optical propagation models, based on the Fresnel approximation, incorporate the physical

Space Telescopes and Instrumentation 2012: Optical, Infrared, and Millimeter Wave, edited by Mark C. Clampin, Giovanni G. Fazio, Howard A. MacEwen, Jacobus M. Oschmann, Jr., Proc. of SPIE Vol. 8442, 84424Q
 · doi: 10.1117/12.926663

characteristics of the Lyot coronagraph elements, mirror surfaces, the deformable mirror, and the CCD imager. Since the underlying physics is not in question, the accuracy of our model predictions is essentially a test of the fidelity of our physical descriptions of the coronagraph elements. These models consistently predict laboratory contrast performance within ~15%, based on prior demonstrations on the HCIT, including TPF-C Milestones #1 and #2, and on more recent coronagraph demonstrations at 20% bandwidth (BW) in support of the ACCESS study.

1.2 Summary of accomplishments

In a nutshell, we have developed a software package that integrates mask design, wavefront sensing and control, dark field nulling procedures, and real-time testbed control – and have used it for the following activities.

1. Designed a Lyot coronagraph mask with contrast performance consistent with requirements for an exoplanet coronagraphic imaging mission, using the design package to simultaneously optimize the focal plane occulter profile and wavefront phase with a single deformable mirror.
2. Manufactured the mask with a deposition facility and calibration methods developed in our laboratory.
3. Demonstrated the hybrid Lyot coronagraph on the High Contrast Imaging Testbed (HCIT), with measured raw contrasts at 3 λ_0/D inner working angles (IWAs) that exceed other published results of which we are aware in spectral bandwidths up to 20%.
4. Demonstrated, for the first time, high contrast wavefront sensing and control in 6.5% BW filters, as one further step towards efficient broadband nulling that will be required for space mission operations.
5. Traced, through model analysis and inspection of fabrication hardware, a calibration error that posed the dominant limitation in our achieved contrast. The error has been corrected and a new mask has been fabricated, ready for future demonstrations of image contrast of a few $\times 10^{-10}$ over a 20% BW.
6. And finally, we have designed a new class of circular hybrid masks, now with 2.5 λ_0/D IWA and BWs of 18%, 24%, and 27%, to be further developed, fabricated, and demonstrated in a future effort.

2. CORONAGRAPH MASKS

Among the four major coronagraph types studied by ACCESS, the complex apodized Lyot coronagraph provides laboratory performance among the best available with today's technology. We seek to advance this technology through new designs and laboratory validations.

2.1 Mask design

Our initial approach was to create an attenuation profile with a prescribed band-limited form[7] as a single thickness-profiled metallic layer on glass, while accepting the resulting phase shifts that necessarily accompany attenuation in real materials. In general, these parasitic phase shifts violate the criteria for band-limited coronagraph masks, and further, real materials exhibit significant dispersion in optical properties over spectral bandwidths up to 20% that are of interest for exoplanet astronomy. The complex apodization approach [8,9] provides a measure of control over phase by adding a non-absorbing thickness-profiled dielectric layer. These new Lyot masks are composed of one metal layer and one dielectric layer superimposed on a glass substrate.

This provides an additional degree of freedom for the problem of speckle suppression over a range of wavelengths. Integrated into a single design algorithm, the thickness profiles of the metal and dielectric layers as well as the actuator settings on a deformable mirror are treated simultaneously as free parameters. Hence, our multilayer thin film interference code (which generates thickness profiles to match specified attenuation and phase profiles) is combined with our wavefront control optimization code (which finds the optimal deformable mirror settings for optical propagation in a realistic coronagraph). All computations are carried out within the Fresnel approximation. Our seamless code, written entirely in Python, has been cross checked for the case of our hybrid Lyot designs with the publicly-available PROPER code[10], demonstrating agreement to within computer rounding errors. Starting with a band-limited design for the real and imaginary parts of the occulter attenuation profile at the 800 nm central wavelength, the code generates physically realizable design adjustments against criteria that balance spectral bandwidth, contrast, inner working angle, and overall throughput (Figure 1). For this work, the mask has been dimensioned for a 3 λ_0/D inner working angle in an f/31.25 beam, corresponding to the HCIT (Figure 6) with a 48-mm diameter pupil stop at the deformable mirror. Predicted performance is shown in Figure 2.

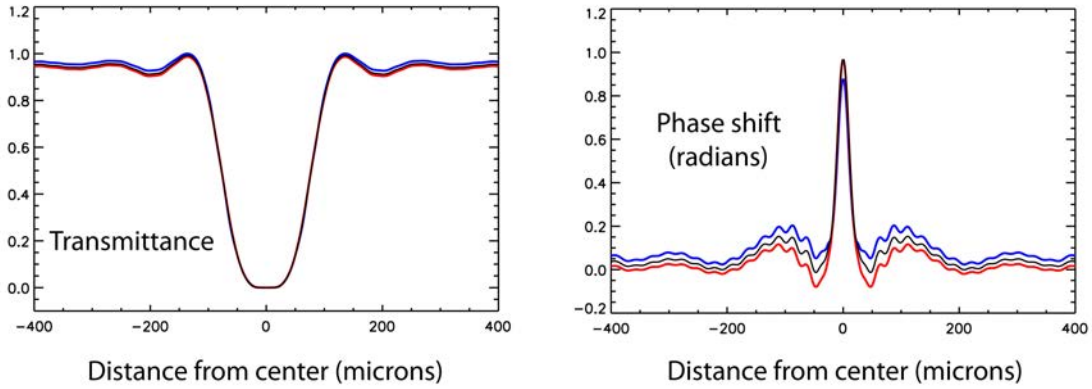

Figure 1. Attenuation and phase shift profiles for the hybrid occulter mask. At left, the attenuation profile reaches 50% transmittance at 3 λ_0/D from center at the central wavelength λ_0 = 800 nm. At right, the transmitted phase profile. Transmittance and phase profiles are shown at three wavelengths: 720 nm (blue curve), 800 nm (black), and 880 nm (red curve). Physical dimensions are scaled to an f/31.25 beam, for which fλ_0/D = 25 microns at 800 nm.

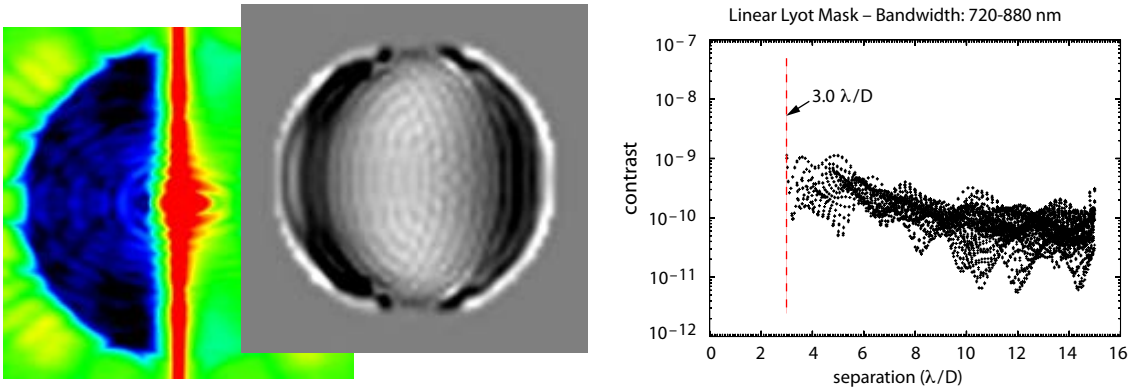

Figure 2. Predicted performance of the hybrid linear Lyot coronagraph, computed with the design software for the mask, a software package that is also used for real-time wavefront sensing and control in the coronagraph experiment. At left, the simulated dark half-field, extending from 3 λ_0/D to a radius of 15 λ_0/D. Center, the corresponding phase setting of the deformable mirror. At right, the pixel-by-pixel contrast over the targeted dark field. Predicted contrast is 2×10^{-10} in both the inner dark field (3-4 λ_0/D) and averaged over the outer (3-15 λ_0/D) dark field areas.

2.2 Mask fabrication

On the fabrication side, we have developed the deposition hardware and procedures for the focal plane mask. The metal and dielectric layers are deposited by vacuum evaporation in the facility shown in Figure 3. A 15-micron slit, made at JPL's MicroDevices Laboratory, is mounted close to the fused silica substrate on a computer controlled linear translation stage. The substrate is scanned behind the slit in 1-micron steps, with dwell times at each step specified to generate the desired thickness profiles. The process is monitored in real time, as indicated in Figure 4. Figure 5 is a photo of a mask fabricated to this design. The mask also incorporates alignment and thickness calibration marks for monitoring and calibration of the manufacturing process.

Figure 3. Fabrication of the two-layer Lyot mask. At left, the linear focal plane mask is formed by vacuum deposition of nickel and cryolite, the raw materials shown at top. At right, the vacuum thin film deposition system with an electron beam source for metal deposition, a thermal evaporation source for the dielectric, and a computer controlled mechanism for movement of the substrate behind the slit deposition mask.

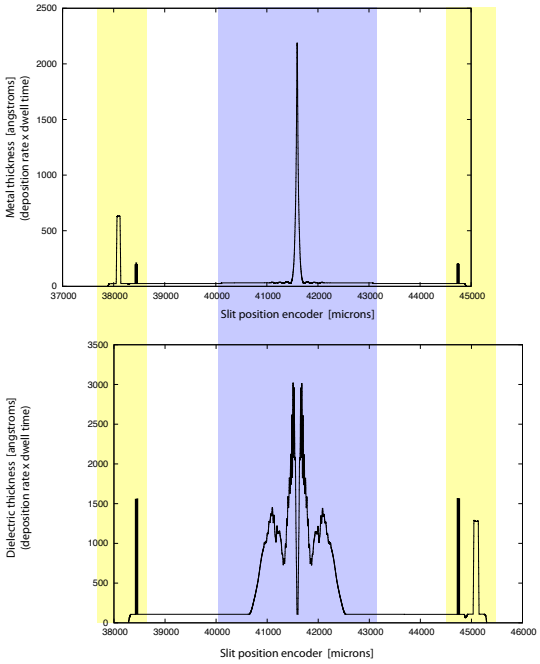

Figure 4. The deposition process is monitored in real time. These two plots show the thickness profiles, built up as the slit makes 50-60 passes in one-micron steps, each pass incrementally increasing the layer thickness by an amount proportional to the product of deposition rates and dwell times. The plots show the final thicknesses at the completion of the metal deposition (top) and the dielectric deposition (bottom). Highlighted in blue are the active areas of the hybrid Lyot focal plane mask, with a narrowly peaked, nearly band-limited metal profile, and a dielectric profile that tailors the phase shifts in the mask. Highlighted in yellow are the alignment fiducial marks. Also seen are the new thickness calibration features deposited to the left of the pattern in the metal layer, and to the right of the pattern in the dielectric.

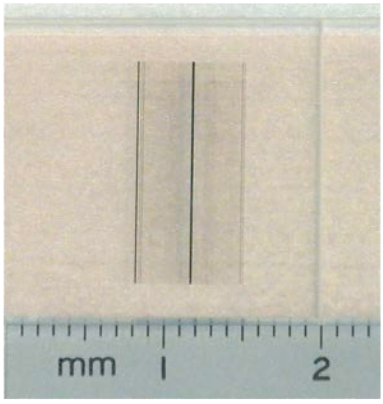

Figure 5. Photograph of the complex apodization Lyot mask, composed of thickness profiled layers of metal and dielectric superimposed on a fused silica substrate with a millimeter scale for comparison. The OD pattern is clearly seen, including the central peak and alignment fiducial marks. The metal thickness calibration mark is seen at the far left. The dielectric calibration mark, at the far right, can be seen in the phase measuring microscope. Close inspection of these fiducial marks indicate that the slit motions were within one micron of the commanded positions for the entire deposition run, and that the metal and dielectric thicknesses were correct to within thickness measurement errors of five percent. This mask was fabricated in January 2012 with an improved calibration procedure.

3. LABORATORY DEMONSTRATIONS

The optical layout of the HCIT Lyot table[6] during these TDEM experiments is shown in Figure 6. The optical table is operated in a vacuum chamber evacuated to ~10 milliTorr levels.

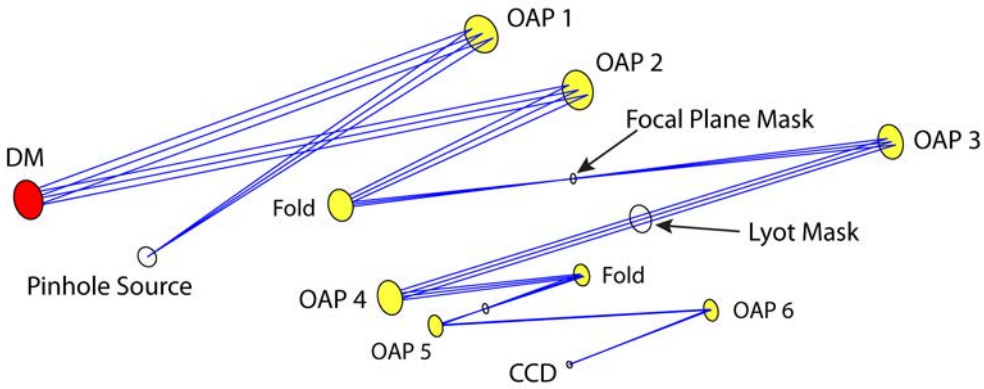

Figure 6. Optical layout of the HCIT Lyot coronagraph table. The optical elements in the optical path, starting from the source, are as follows. The source of continuum light illuminates OAP 1, the first of six off-axis paraboloidal (OAP) mirrors, which collimates the beam. The beam passes to the deformable mirror (DM), where a 48 mm diameter aperture stop defines the pupil of the system. The DM is from Xinetics, with a square array of actuators spaced on a 1-mm pitch, such that 1810 actuators are active within the pupil aperture. The collimated light is then focused by OAP 2 and folded by a flat mirror, passing to the focal plane where the focal plane coronagraph mask is located. The beam is collimated by OAP 3 on its way to the Lyot stop, which is located in a pupil plane conjugate to the deformable mirror. The collimated beam is then brought to a focus by OAP 4 to create the high-contrast coronagraph image, where a field stop is positioned to reduce scattered light. A camera, formed by OAPs 5 and 6, then magnifies and projects the coronagraph image onto the CCD focal plane.

3.1 Coronagraph demonstrations

Our laboratory procedures have been exercised and validated in previous demonstrations in the HCIT, including TPF-C Milestone #2. A flavor of the electric field conjugation method (EFC)[11] is used and iterated as necessary, as follows.

For each filter in a set of optical filters that sample the specified overall wavelength range, and starting with a nominally flat surface figure setting on the DM: (a) take the set of contrast field images with the initial DM setting and estimate the contrast average across the specified wavelength range; (b) take images in each filter for each of four "probe" DM settings (consisting of small deterministic surface figure deviations from the initial DM setting) and measure their effects across the specified range; (c) use these data to compute the complex electric field in the target dark field region; and then (d) calculate and apply a single new DM setting that will reduce the energy over the dark field averaged over all filters, thus establishing a new "initial DM setting" in preparation for the next iteration, which is a loop back to step (a). A typical integration time for an individual image is about ten seconds, and one complete wavefront sensing and control cycle, including overhead for CCD readouts, data handling and computations for a 20% band, typically takes 10-15 minutes.

Table 1. The set of optical bandpass filters used for these demonstrations. Listed are filter IDs for reference, the spectral passband measured to the half-transmittance wavelengths, and the spectral bandwidth as a percentage of the central wavelength.

Filter ID	FWHM wavelength range	Bandwidth ($\delta\lambda/\lambda_0$)
1	719.4 – 735.1 nm	2.2%
2	761.5 – 776.5 nm	2.0%
3	774.7 – 790.1 nm	2.0%
4	790.9 – 806.7 nm	2.0%
5	806.7 – 822.8 nm	2.0%
6	823.1 – 838.6 nm	1.9%
7	864.2 – 879.9 nm	1.8%
8	720.7 – 769.3 nm	6.5%
9	771.5 – 821.2 nm	6.2%
10	823.5 – 878.7 nm	6.5%

Quoted contrast vales are the ratio of signal/second averaged over the dark field to the signal/second averaged over the central λ/D diameter of the star's point spread function. The star signal is obtained with the coronagraph mask offset by a few λ/D to allow the starlight to pass with little attenuation through a highly transmitting area of the mask, with the Lyot stop in place. Since the star is very bright, it is measured it with the aid of a calibrated attenuator. With the coronagraph mask returned to a position well centered on the star, images are taken of the dark field of speckles surrounding the suppressed star. The dimensions of the target area, illustrated in Figure 2, are defined as follows: (a) A dark outer (D-shaped) field extending from 3 to 15 λ_0/D, representing the high contrast field of view on the sky, is bounded by a straight line that passes 3 λ_0/D from the star at its closest point, and by a circle of radius 15 λ_0/D centered on the star. (b) An inner area within the foregoing dark field, representing contrast at the inner working angle of 3 λ_0/D, is bounded by a square box, each side measuring λ_0/D, such that one side is coincident with the foregoing straight line and centered on the closest point to the star. The image is corrected for the mask attenuation profile by dividing it out, and the image is normalized to the star brightness. This contrast image is averaged over the defined high-contrast fields to produce the quoted contrast values. In the case of multiple filters used to represent the full bandwidth (e.g., five 2% filters sampling an overall 20% spectral band), the contrast is the average of contrasts in the individual bands for a single given setting of the DM. To probe the reliability of our measurements, we have taken hundreds of repeated nulling and contrast measurement cycles for each of the five experiments summarized below. Six representative consecutive cycles have been extracted from each of these experiments and listed in the following contrast tables. For two of the experiments, we carried out the contrast estimations with the star at three different positions on the linear occulting mask in order to test whether local irregularities in the mask might be significant.

3.2 Experimental Results

Here we collect nine data sets representative of the experimental results of our 12-week HCIT run in May-July 2011. These each include measured contrast for six consecutive iteration cycles, sufficient to establish a statistically significant result. We include the following data sets.

Data set 1. Contrast demonstration in a single 2% band centered at 800 nm (Filter 4) is shown in Table 2. This narrowband series establishes the limiting contrast for the system including both incoherent scattered background and unsuppressed coherent starlight, with a minimum of spectral bandwidth and chromatic effects. The average contrast in the inner 3-4 λ_0/D field is 3.42 (± 0.05) $\times 10^{-10}$, while the average in the outer 3-15 λ_0/D field is 2.25 (± 0.03) $\times 10^{-10}$. The mean contrast is better than 1×10^{-9} with a confidence level > 99%.

Data sets 2,3,4. Contrast over a 10% band was obtained in five contiguous 2% spectral bands (Filters 2,3,4,5,6), in a manner nearly identical to that of TPF-C Milestone #2. We have selected three sets of six nulling cycles each, with results collected in Table 3. Each set was taken at a different position on the same linear Lyot mask, with the location of the star along the occulter shifted from the others by more than 3 λ_0/D. The average contrast in the inner 3-4 λ_0/D field is 6.72 (± 1.58) $\times 10^{-10}$, while the average in the outer 3-15 λ_0/D field is 6.14 (± 0.67) $\times 10^{-10}$. The mean contrast is better than 1×10^{-9} with a confidence level > 98%.

Data sets 5,6,7. Contrast over a 20% band was obtained in five 2% spectral bands (Filters 1,2,4,6,7) spanning 720-880 nm. We have selected three sets of six cycles each, with results collected in Table 4. Each set was taken at a different position on the same linear Lyot mask, with the location of the star on the occulter shifted from the others by more than 3 λ_0/D. The average contrast in the inner 3-4 λ_0/D field is 2.30 (± 0.30) $\times 10^{-9}$, while the average in the outer 3-15 λ_0/D field is 1.79 (± 0.16) $\times 10^{-9}$.

Data set 8. A contrast demonstration in a single 6.2% band (Filter 9) centered at 800 nm is shown in Table 5. Both nulling and contrast scoring were carried out with just this single filter, demonstrating high contrast wavefront control in a spectral band significantly larger than 2% and indicating that our wavefront sensing and control model has successfully accounted for chromatic effects at the demonstrated contrast level. The average contrast in the inner 3-4 λ_0/D field is 5.85 (± 0.66) $\times 10^{-10}$, while the average in the outer 3-15 λ_0/D field is 4.25 (± 0.21) $\times 10^{-10}$. The mean contrast is better than 1×10^{-9} with a confidence level > 99%.

Data set 9. Contrast over a 20% band was measured in the three 6.5% filters (Filters 8,9,10) and listed in Table 6, with the caveat that the longest wavelengths in the 720-880 nm band are somewhat underrepresented (due to a non-uniform supercontinuum spectrum in Filter 10) when averaging the contrast in all three spectral bands. The average contrast in the inner 3-4 λ_0/D field is 1.84 (± 0.35) $\times 10^{-9}$, while the average in the outer 3-15 λ_0/D field is 1.72 (± 0.11) $\times 10^{-9}$. This data set demonstrates that the chromatic effects across the 6.5% spectral bands are sufficiently well represented in our model to produce results comparable to the earlier nulling in 2% bands, setting the stage for highly efficient dark field nulling in the future with single filters as broad as 20%.

Table 2. Dark field nulling was carried out with a single 2% filter centered at a wavelength of 800 nm. Listed are the raw contrasts measured in the inner and outer fields for six consecutive nulling iterations.

Date & Time	Inner Field ($\times 10^{-9}$)	Outer Field ($\times 10^{-9}$)
16 Jul 2011 – 13:07	0.401	0.227
16 Jul 2011 – 13:19	0.317	0.226
16 Jul 2011 – 13:31	0.381	0.224
16 Jul 2011 – 13:43	0.327	0.225
16 Jul 2011 – 13:55	0.271	0.229
16 Jul 2011 – 14:07	0.353	0.221

Table 3. Contrast over a 10% spectral band, sampled with 5 × 2% FWHM filters. Dark field nulling was carried out using five filters with contiguous 2% passbands spanning the 760-840 nm spectral range. Listed are the measured contrasts in the inner field (a square box extending from 3 to 4 λ_0/D) and averaged over an outer field (extending to a radius of 15 λ_0/D) for six consecutive nulling iterations. The three sets of data are taken at different positions along the linear focal plane mask. Offset between the set at top and at center is 1.00 mm = 40 λ_0/D. The set at bottom is displaced by an additional 0.92 mm = 37 λ_0/D.

Occulter y-coordinate = 2.270 mm

Date & Time	Inner Field ($\times 10^{-9}$)	Outer Field ($\times 10^{-9}$)
16 Jul 2011 – 5:03	0.610	0.519
16 Jul 2011 – 5:32	0.654	0.523
16 Jul 2011 – 6:02	0.620	0.520
16 Jul 2011 – 6:32	0.562	0.520
16 Jul 2011 – 7:03	0.564	0.522
16 Jul 2011 – 7:33	0.662	0.523

Occulter y-coordinate = 1.270 mm

Date & Time	Inner Field ($\times 10^{-9}$)	Outer Field ($\times 10^{-9}$)
26 Jul 2011 – 7:51	0.986	0.660
26 Jul 2011 – 8:18	0.971	0.664
26 Jul 2011 – 8:44	0.658	0.656
26 Jul 2011 – 9:11	0.815	0.654
26 Jul 2011 – 9:39	0.831	0.665
26 Jul 2011 – 10:14	0.914	0.669

Occulter y-coordinate = 0.350 mm

Date & Time	Inner Field ($\times 10^{-9}$)	Outer Field ($\times 10^{-9}$)
28 Jul 2011 – 15:23	0.544	0.663
28 Jul 2011 – 15:55	0.573	0.662
28 Jul 2011 – 16:27	0.539	0.655
28 Jul 2011 – 17:43	0.569	0.651
28 Jul 2011 – 18:19	0.513	0.665
28 Jul 2011 – 18:51	0.516	0.653

Table 4. Contrast over a 20% spectral band sampled with 5 × 2% FWHM filters. Dark field nulling was carried out using five 2% filters spaced across the 720-880 nm spectral range. Listed are the measured contrasts in the inner field (a square box extending from 3 to 4 λ_0/D) and averaged over an outer field (extending to a radius of 15 λ_0/D) for six consecutive nulling iterations. As in Table 3 above, three sets of data are taken at different positions along the linear focal plane mask.

Occulter y-coordinate = 2.270 mm

Date & Time	Inner Field ($\times 10^{-9}$)	Outer Field ($\times 10^{-9}$)
11 Jul 2011 – 20:23	2.35	1.84
11 Jul 2011 – 20:48	2.15	1.83
11 Jul 2011 – 21:13	2.57	1.82
11 Jul 2011 – 21:38	2.47	1.79
11 Jul 2011 – 22:04	2.44	1.83
11 Jul 2011 – 22:29	2.28	1.83

Occulter y-coordinate = 1.270 mm

Date & Time	Inner Field ($\times 10^{-9}$)	Outer Field ($\times 10^{-9}$)
25 Jul 2011 – 21:53	2.68	1.63
25 Jul 2011 – 22:25	2.51	1.61
25 Jul 2011 – 22:56	2.60	1.62
25 Jul 2011 – 23:28	2.60	1.57
26 Jul 2011 – 0:00	2.50	1.54
26 Jul 2011 – 0:32	2.65	1.52

Occulter y-coordinate = 0.350 mm

Date & Time	Inner Field ($\times 10^{-9}$)	Outer Field ($\times 10^{-9}$)
28 Jul 2011 – 5:30	1.97	1.97
28 Jul 2011 – 5:58	1.82	1.94
28 Jul 2011 – 6:26	1.89	1.95
28 Jul 2011 – 6:55	1.92	1.93
28 Jul 2011 – 7:23	2.09	1.96
28 Jul 2011 – 7:51	1.92	1.97

Table 5. Dark field nulling was carried out with a single 6.5% filter spanning the 772–821 nm wavelength range. Listed are the measured contrasts in the inner and outer fields for six consecutive nulling iterations. Contrast performance matches that in the 10% demonstration (Table 3), but in a single filter that gathers more photons/second than a comparable set of three 2% filters, for a quicker nulling sequence as would be desired in a space mission where calibration time and stellar flux are limited.

Date & Time	Inner Field ($\times 10^{-9}$)	Outer Field ($\times 10^{-9}$)
9 Aug 2011 – 5:23	0.575	0.508
9 Aug 2011 – 5:30	0.522	0.507
9 Aug 2011 – 5:37	0.494	0.509
9 Aug 2011 – 5:43	0.637	0.512
9 Aug 2011 – 6:00	0.632	0.515
9 Aug 2011 – 6:17	0.650	0.505

Table 6. Contrast over a 20% spectral band samples with 3 × 6.5% FWHM filter passbands spanning the 720-880 nm spectral range. Listed are the measured contrasts in the inner field (a square box extending from 3 to 4 λ_0/D) and averaged over an outer field (extending to a radius of 15 λ_0/D) for six consecutive nulling iterations. Broad spectral bands (that gather more photons/second distributed among fewer filters) enable a quicker nulling sequence, as would be desired in a space mission where calibration time and stellar flux are limited.

Date & Time	Inner Field ($\times 10^{-9}$)	Outer Field ($\times 10^{-9}$)
8 Aug 2011 – 5:20	1.84	1.72
8 Aug 2011 – 5:34	1.84	1.71
8 Aug 2011 – 5:48	1.86	1.70
8 Aug 2011 – 6:01	1.87	1.72
8 Aug 2011 – 6:15	1.85	1.73
8 Aug 2011 – 6:29	1.77	1.71

3.3 Discussion

Based on past experiments on the HCIT, we expect good agreement between the measured (Tables 2–6) and predicted (Figure 2 and its caption) coronagraph contrast. Given our evident disagreement in the 20% bandpass, we undertook a number of empirical investigations of the most likely possible causes during our May-July 2011 run. Several lines of evidence led us to conclude that the Lyot mask had an incorrect dielectric thickness. As indicated in Figure 4 and the surrounding text, the thicknesses of the individual metal and dielectric layers are monitored during deposition with a quartz crystal microbalance. A calibration factor is needed to relate the thickness deposition rates on the crystal monitor versus the occulter substrate. An error in these calibration factors would result in layer thickness profiles in error by a constant of proportionality. We used our models to predict the effects of such errors for either the metal or dielectric films, under the same constraints as the testbed nulling experiment, and were quickly led to suspect that the calibration factor for the dielectric layer was in error by about 20%. Our suspicion was confirmed by microscope inspection of the 15-micron slit used for the mask deposition. The width of the slit narrowed significantly during the dielectric deposition due to buildup of the material on the sides of the slit.

We revised our calibration and fabrication processes to ensure that this particular problem will not recur in future work. We have added thickness calibration "witness bars" to the deposition pattern, as indicated in Figures 4 and 5, to allow after-the-fact measurement and verification of the correct thickness factors in the finished Lyot mask. A new mask has been fabricated with the improved calibration in January 2012, and we expect to fabricate additional masks as time permits in preparation for a possible future high contrast run in the HCIT.

4. NEW CIRCULAR LYOT MASK DESIGNS

We continue our exploration of the design space for hybrid Lyot masks using the integrated design software package described above. We now report a preliminary investigation of high performance circular Lyot masks with inner working angles as small as 2.5 λ_0/D and spectral bandwidths greater than 18%.

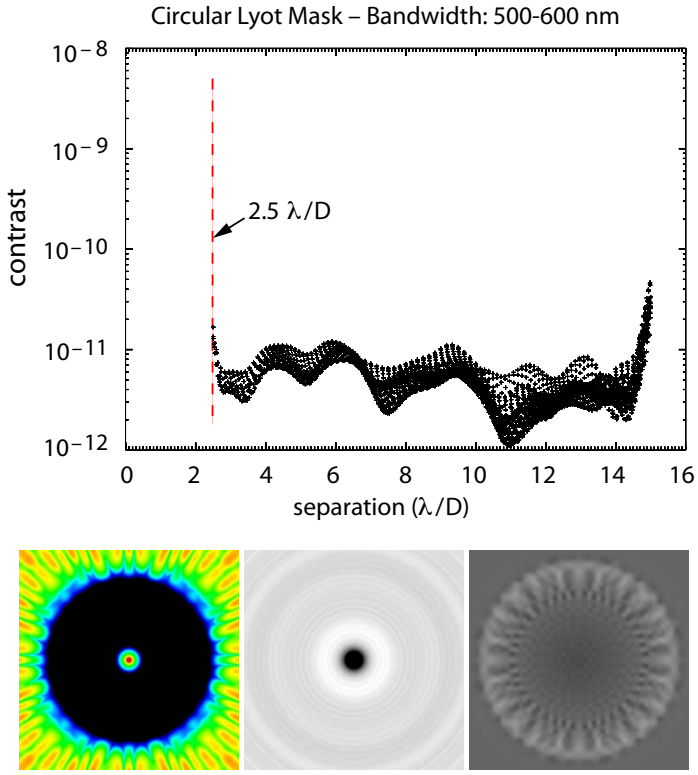

Figure 13. Predicted performance for a newly designed circular hybrid Lyot mask. Inner working angle is 2.5 λ_0/D. The design optimization is carried out by varying thickness profiles of the metal and dielectric layers in concert with the wavefront control enabled by a single DM with a 48×48 array of actuators. Note that a full 360^O dark field has been created with a single deformable mirror. Contrast in the 500-600 nm ($\delta\lambda/\lambda_0$ = 18%) spectral band is 5.3×10^{-12} in both the inner 2.5-3.5 λ_0/D annulus and averaged across the entire dark field extending from radii of 2.5 to 15 λ_0/D. The three images at bottom are: (left to right) the high contrast dark field displayed on a logarithmic contrast stretch from $10^{-11}$to 10^{-7}, the intensity transmittance of the occulting mask on a linear scale from 0 to 1, and the DM figure pattern extending to ±40 nm of surface displacement.

We present one example, designed for a 2.5 λ_0/D inner working angle and an 18% spectral bandwidth centered on λ_0 = 550 nm. Figure 13 illustrates dark field contrast better than 1×10^{-11} over the entire dark field extending from 2.5 to 15 λ_0/D, and over the 500–600 nm wavelength band. Further, we note that this full dark field has been achieved with relatively small strokes of a single 48×48 actuator DM, by exploiting the ability of a DM to control the real and imaginary parts of the complex wavefront over half the controllable area (in this case, the central half of the controllable area, rather than the right or left half). Comparable results have been obtained for larger bandwidths up to 27% (475-625 nm) with predicted contrasts better than 1×10^{-9} over the entire dark field. The fabrication of these designs will be pursued as opportunities arise in the future.

5. DIFFERENCES BETWEEN LABORATORY DEMONSTRATIONS AND FLIGHT

There are several important differences between the laboratory demonstration reported here and the ACCESS flight implementation. Each is addressed briefly below.

Starlight: In a space coronagraph, the spectrum of light illuminating the coronagraph would closely resemble black body radiation. The spectral distribution produced by our laboratory light source (a fiber-coupled supercontinuum laser) is smooth, but nevertheless with variations by up to 50% in brightness vs. wavelength across a 20% spectral band.

As such, a single filter spanning a 20% spectral band does not provide a reliable test of the contrast over the entire spectral band. Our original preference was to measure the contrast in a set of three contiguous 6.5% passbands that span the full 20% bandwidth, and an excellent set of three filters was purchased. The filters are mounted in a selection wheel within the supercontinuum source module outside the vacuum chamber, so that they can be interchanged easily without disrupting the optical system in any way. Contrast estimates from each of the 6.5% bands are individually calibrated against the photometry reference and averaged to construct the contrast metric over the full 20% spectral band. This procedure effectively corrects for spectral variations in the supercontinuum source.

However, we were unable to find an alignment for the longest of the three 6.5% filters that fairly represented a uniform light source at the longest wavelengths in the 20% band, so we decided instead to sample the contrast over the full 20% band in five 2% bands. The longest and shortest wavelengths are therefore well represented, and a weighted average with this evenly-spaced picket fence of five passbands provides an accurate estimate of the overall 20% contrast. In this TDEM run, the set of three 6.5% filters were used to demonstrate broadband nulling, while a set of five 2% filters was used as our most accurate method to score the final 20% contrast.

The supercontinuum source provides a photon flux that is comparable to or somewhat brighter than the target stars to be observed by the mission (e.g., a star with visual magnitude V=1 observed with a 1.5 meter telescope). Our objective is to determine the achievable broadband contrast, which is independent of the source intensity, so a bright source is a convenience that does not compromise the integrity of the demonstration.

Finally, unlike the light collected by a telescope from a target star, the light is coherent across the 5-micron source pinhole, and therefore equivalent to a star sufficiently distant to have a negligible angular diameter. However, it projects an intensity that is slightly non-uniform across the pupil; typically this is a center-to-edge "droop" of a few percent corresponding to the diffraction pattern from a 5-micron source pinhole. This small non-uniformity has negligible effect on the final contrast if it is accounted for in the wavefront control algorithm, and would result in a finite but insignificant loss of contrast if it were ignored in the control algorithm.

Spacecraft dynamics: A control system is required in flight to stabilize the light path against motions of the spacecraft. The dominant effects of spacecraft dynamics are jitter of the star image on the coronagraph focal plane mask and beam walk in the optics upstream of the focal plane mask. For a specific example, the ACCESS analysis showed that for fourth-order coronagraphs (including Lyot, vortex, and pupil mapping coronagraphs) with an inner working angle of $3\lambda_0/D$, pointing errors needed to be less than $\pm 0.03\ \lambda_0/D$ to limit the corresponding contrast degradation to less than 2×10^{-10}. The ACCESS analysis has shown that the required pointing stability can be achieved in space with current high Technology Readiness Level (TRL) systems. Scaled to the HCIT, the pointing control requirement corresponds to an ability to center the occulting mask on the "star" within 1 μm, or about 0.23 pixel when projected to the CCD focal plane.

The laboratory demonstration requires the passive stability of the testbed, including the centration of the star on the occulter as one example, which is untraceable to spacecraft dynamics. In practice, the HCIT often exhibits alignment drifts that are larger than expected in the space environment. As such we must rely on favorable periods of thermal and mechanical stability of the HCIT.

Single deformable mirror: The demonstrations were carried out with a single DM, which allows the control of phase and amplitude in the complex wavefront over one half of the coronagraph field described above. In flight, it is expected that a pair of DMs will be used, in series, to generate a full (two-sided) dark field extending to the Nyquist limits of DM control, with the added advantages of a deeper contrast field and better broadband control.

6. CONCLUSIONS

This TDEM program has provided an opportunity for significant progress in the design and fabrication of a coronagraph flight instrument. We have demonstrated raw imaging contrast that exceeds other published results that we are aware of

at 3 λ_0/D inner working angles, and over spectral bandwidths of 2, 6, 10, and 20%. The TDEM experience has allowed us to upgrade our design and fabrication process, and has proven the value of a seamless software approach that encompasses mask design, wavefront sensing and control, optical tolerancing and diagnostics, and real-time testbed control. We have corrected our fabrication processes and have produced a new hybrid Lyot mask for testbed opportunities that may arise in the future, with full expectations that it will perform at the contrast levels of $\sim 5\times10^{-10}$ over the 3-15 λ_0/D dark field. And we have embarked on the design of circular hybrid Lyot masks that promise ultimately better performance and efficiency compared to the linear masks in this report. Our experience has opened new avenues for future progress, and we are optimistic that significant further advances will follow.

ACKNOWLEDGEMENTS

We thank Peter Lawson and the TDEM Technology Assessment Committee for their valuable comments and critical review of this work. We acknowledge the support provided by Brian Kern, Albert Niessner, and the ExEP HCIT infrastructure team during the laboratory demonstrations. The research described in this paper was carried out at the Jet Propulsion Laboratory, California Institute of Technology, under a contract with the National Aeronautics and Space Administration.

REFERENCES

[1] Trauger, J. *et al*., "ACCESS – A Concept Study for the Direct Imaging and Spectroscopy of Exoplanetary Systems," in *Pathways towards Habitable Planets, ASP Conf. Series* **430***,* 375, 2010; and *Proc. SPIE* **7731,** 773128 (2010).

[2] Trauger, J. *et al*., "ACCESS – A space coronagraph concept for direct imaging and spectroscopy of exoplanetary systems," Public version of the Final Report to the NASA Astrophysics Strategic Concept Studies Program (2009).

[3] Trauger, J.T. and W.A. Traub, "A laboratory demonstration of the capability to image an Earth-like extrasolar planet," *Nature* **446**, 771 (2007).

[4] Trauger, J. *et al.*, "TPF-C Milestone #1 Report," JPL Document D-35484 (2006).

[5] Kern, B. *et al.*, "TPF-C Milestone #2 Report," JPL Document D-60951 (2008).

[6] Trauger, J., A. Give'on, B. Gordon. B. Kern, A. Kuhnert, D. Moody, A. Niessner, F. Shi, D. Wilson, and C. Burrows, "Laboratory demonstrations of high-contrast imaging for space coronagraphy," *Proc. SPIE* **6693**, 66930X (2007).

[7] Kuchner, M., and W. Traub, "A coronagraph with a band-limited mask for finding terrestrial planets," *Astrophys. J.* **570**, 900 (2002).

[8] Moody, D., B.L. Gordon, and J. Trauger, "Design and demonstration of hybrid Lyot coronagraph masks for improved spectral bandwidth and throughput," *Proc. SPIE* **7010**, 70103P (2008).

[9] Trauger, J. *et al*., "A hybrid Lyot coronagraph for the direct imaging and spectroscopy of exoplanet systems: recent results and prospects" *Proc. SPIE* **8151**, 81510G (2011).

[10] Krist, J.E., "PROPER: an optical propagation library for IDL," *Proc. SPIE* **6675**, 66750P (2007).

[11] Give'on, A., B. Kern, S. Shaklan, D. Moody, and L. Pueyo, "Broadband wavefront correction algorithm for high-contrast imaging systems," *Proc. SPIE* **6691**, 66910A (2007).